

## Calculation of isotope shifts and King-plot nonlinearities in $\text{Ca}^+$

A. V. Viatkina <sup>1,2</sup>, V. A. Yerokhin <sup>3</sup>, and A. Surzhykov <sup>1,2</sup>

<sup>1</sup>*Technische Universität Braunschweig, 38106 Braunschweig, Germany*

<sup>2</sup>*Physikalisch-Technische Bundesanstalt, 38116 Braunschweig, Germany*

<sup>3</sup>*Max-Planck-Institut für Kernphysik, Saupfercheckweg 1, 69117 Heidelberg, Germany*



(Received 12 June 2023; accepted 19 July 2023; published 4 August 2023)

Many-body perturbation theory is implemented to calculate the isotope shifts of  $4s$ ,  $4p_{1/2}$ ,  $4p_{3/2}$ ,  $3d_{3/2}$ , and  $3d_{5/2}$  energy levels of  $\text{Ca}^+$  for even isotopes  $A = 40, 42, 44, 46, 48$ . The results are presented for mass shift and field shift, as well as for higher-order field shifts, quadratic mass shift, nuclear polarization correction, and the cross term between field and mass shifts. Additionally, we examine King-plot nonlinearities introduced by higher-order isotope-shift corrections to the combinations of  $3d_{3/2} \rightarrow 4s$ ,  $3d_{5/2} \rightarrow 4s$ , and  $4p_{1/2} \rightarrow 4s$  transitions. For these transitions, second-order mass shift and nuclear polarization correction are identified as the dominant sources of King-plot nonlinearity.

DOI: [10.1103/PhysRevA.108.022802](https://doi.org/10.1103/PhysRevA.108.022802)

### I. INTRODUCTION

High-precision atomic spectroscopy is currently in the spotlight of experimental research, particularly as a means of testing physics beyond the standard model [1–3]. The recent advances in experimental technique allows one to determine atomic transitions with high accuracy, which, in certain cases, reaches 0.1 Hz [4–9]. One of the precision-spectroscopy methods aimed at detecting new interactions is the King-plot analysis; the basic idea was proposed in Refs. [2,10] and later refined in Refs. [3,11,12]. Roughly speaking, the King plot is a plot constructed from normalized isotope shifts of atomic transitions which are measured in a series of isotopes of a given element; such plots can be proven to be linear to a high precision. However, it has been shown that an interaction between the electron cloud and the nucleus mediated by a hypothetical light boson would distort this linearity [2]. Hence, if a nonlinearity in a King plot is detected in the experiment, it could be attributed to a new boson given that any other explanation is ruled out [2]. On the other hand, as one may expect, there are numerous sources of King-plot nonlinearities found already in the framework of the standard model.

Recently, a significant King-plot nonlinearity was discovered in Yb and  $\text{Yb}^+$  transitions [3,13,14] and the efforts of its interpretation are still ongoing, see, e.g., Refs. [13,15]. In contrast, King plots in a succession of  $\text{Ca}^+$  isotopes were found to be linear within experimental uncertainties [16–18]. Isotope shifts were measured for  $4s\ ^2S_{1/2} \rightarrow 4p\ ^2P_{1/2}$  and  $3d\ ^2D_{3/2} \rightarrow 4p\ ^2P_{1/2}$  transitions with accuracy below 100 kHz [19,20], for  $4s\ ^2S_{1/2} \rightarrow 3d\ ^2D_{5/2}$  with accuracy below 10 Hz [16], and for the interval  $3d\ ^2D_{3/2} - 3d\ ^2D_{5/2}$  with  $\sim 20$  Hz accuracy [18]. One can expect that, in the future, the measurement accuracy reaches 1 Hz; in such a case, the King-plot linearity might no longer hold and a careful theoretical examination of the origins of nonlinearity will be needed. In this contribution, therefore, we aim to lay the groundwork for an analysis of the  $\text{Ca}^+$  King-plot nonlinearity.

It should be noted that, as a system intended for isotope-shift spectroscopy,  $\text{Ca}^+$  has several advantages. First, calcium has five even-even stable ( $A = 40, 42, 44, 46$ ) or long-lived ( $A = 48$ ) isotopes, which is a welcome fact for building a King plot. Isotopes with zero nuclear spin are preferred for King-plot analysis because their spectra lack hyperfine splitting. Second, the electronic structure and atomic transitions of  $\text{Ca}^+$  are theoretically well understood given its alkali-like electronic configuration. Third,  $\text{Ca}^+$  is a convenient object for experimental study: as was mentioned above, a series of experiments has already been conducted to determine several of its atomic transitions with high accuracy [16–20], with a realistic possibility for future improvement.

In the present work, we calculate the main contributions to isotope shift in  $\text{Ca}^+$  ions and evaluate their impact on King-plot linearity. The relativistic units ( $\hbar = c = m = 1$ ) are used throughout this paper unless explicitly specified. The paper is structured as follows. In Sec. II we introduce the theoretical origins of isotope shift terms: we discuss mass shift (Sec. II A), field shift (Sec. II B), nuclear polarization, and the field- and mass-shift cross terms (Sec. II C). The total isotope shift (the sum of all considered contributions) is presented in Sec. II D. In Sec. III the specific methods for many-body calculations are laid out, which we subsequently use in Sec. IV to evaluate each of the isotope shift terms. Finally, we discuss  $\text{Ca}^+$  King plots and their nonlinearity in Sec. V and summarize our results in Sec. VI.

### II. ISOTOPE SHIFT: THEORY

In the first-order approximation, the isotope shift of an energy level in the  $i$ th isotope with respect to a reference isotope  $a$  can be written as

$$\Delta E_{ia} = K \left( \frac{m}{M_i} - \frac{m}{M_a} \right) + F (R_i^2 - R_a^2), \quad (1)$$

where  $m$  is the electron mass and  $M_j$  denote nuclear masses ( $j = a, i$ ). Here, we introduce a dimensionless nuclear charge

radius

$$R_j^2 = \langle r^2 \rangle_j / \lambda_C^2, \quad (2)$$

which is a mean-square nuclear charge radius  $\langle r^2 \rangle_j$  divided by (the square of) the reduced Compton wavelength of an electron,  $\lambda_C$ . The first term in Eq. (1) corresponds to *mass shift* (MS) and the second term to *field shift* (FS); the first is the consequence of the change in nuclear mass and the second of the change in nuclear charge distribution between two isotopes. Note that in the first-order approximation (1) the electronic structure constants  $K$  and  $F$  do not depend on the nuclear parameters of the  $i$ th isotope, while they may still implicitly include the parameters of the reference isotope  $a$ . Effectively, Eq. (1) assumes that electronic wave functions do not yet “notice” the change in nuclear mass and the shape between isotopes.

In the present work, we investigate the effects beyond the first-order approximation (1). We take into account that both electronic “constants”  $K$  and  $F$  depend on the isotope  $i$  in question and hence the energy shift can be written as

$$\Delta E_{ia} = K_{ia} \left( \frac{m}{M_i} - \frac{m}{M_a} \right) + F_{ia} (R_i^2 - R_a^2). \quad (3)$$

Below, we will examine the isotope dependence of  $K_{ia}$  and  $F_{ia}$ , treating the mass shift and field shift separately. Moreover, we will consider further contributions to isotope shifts which do not, strictly speaking, belong either to the mass or field shift: nuclear polarization correction and the cross term between the field and mass shifts. At the end, we will show how to extend Eq. (3) to take those additional effects into account. Note that, in this work, we will use the  $^{40}\text{Ca}$  isotope as our reference isotope  $a$  ( $A_a = 40$ ).

### A. Mass shift

Isotope mass shift arises from the difference in nuclear recoil effect between two isotopes. For light atomic systems it is sufficient to describe the nuclear recoil by means of non-relativistic operators [21]. Thus, let us write the Schrödinger Hamiltonian of the atom

$$H = \frac{\vec{P}^2}{2M} + \sum_k \frac{\vec{p}_k^2}{2m} + V_C. \quad (4)$$

Here  $\vec{P}$  refers to the nuclear momentum,  $\vec{p}_k$  to the momentum of the  $k$ th electron. By  $V_C$  we denote the Coulomb potential

$$V_C = - \sum_k \frac{Z\alpha}{|\vec{r}_0 - \vec{r}_k|} + \sum_{k<l} \frac{\alpha}{|\vec{r}_k - \vec{r}_l|}, \quad (5)$$

where  $\alpha$  is the fine-structure constant and  $\vec{r}_0$  and  $\vec{r}_k$  are the position vectors of the nucleus and the  $k$ th electron, respectively. Choosing the center-of-mass reference frame, we obtain  $\vec{P} = - \sum_k \vec{p}_k$  and Eq. (4) becomes [22]

$$H = \sum_k \frac{\vec{p}_k^2}{2m_r} + V_C + \frac{1}{M} V_{\text{SMS}}, \quad (6)$$

where  $m_r = mM/(m+M)$  is the reduced mass. In this equation, the first term is the normal mass shift (NMS) operator

whose effect can be observed already in hydrogen-like systems, while the last term  $V_{\text{SMS}}$  is the many-electron specific mass shift (SMS) operator

$$V_{\text{SMS}} = \sum_{k<l} \vec{p}_k \cdot \vec{p}_l. \quad (7)$$

To further evaluate Eq. (6), we introduce  $\mu = m_r/m$  and shift the variables in Eq. (6) as  $\vec{r} \rightarrow \mu^{-1}\vec{r}$  and, therefore,  $\vec{p} \rightarrow \mu\vec{p}$ . Thereby we obtain

$$H = \mu \left[ \sum_k \frac{\vec{p}_k^2}{2m} + V_C + \frac{\mu}{M} V_{\text{SMS}} \right] \equiv \mu \left[ H_0 + \frac{\mu}{M} V_{\text{SMS}} \right], \quad (8)$$

where  $H_0$  is the nonrelativistic atomic Hamiltonian in the infinite nuclear mass limit. If we denote the eigenfunctions of  $H_0$  as  $\psi_0$ , its eigenvalues as  $E_0$ , and expand the eigenvalues of  $H$  in the powers of  $m/M$ , we obtain the first- and second-order nuclear recoil (or mass-shift) corrections to an electronic energy level

$$\delta E_{\text{MS}}^{(1)} = \frac{m}{M} (-E_0 + K_{\text{SMS}}^{(1)}), \quad (9)$$

$$\delta E_{\text{MS}}^{(2)} = \left( \frac{m}{M} \right)^2 (E_0 - K_{\text{SMS}}^{(1)} + K_{\text{SMS}}^{(2)}). \quad (10)$$

Here, the first- and second-order specific mass shift constants are given by

$$K_{\text{SMS}}^{(1)} = \langle \psi_0 | V_{\text{SMS}} | \psi_0 \rangle, \quad (11)$$

$$K_{\text{SMS}}^{(2)} = \sum_{n \neq 0} \frac{|\langle \psi_0 | V_{\text{SMS}} | \psi_n \rangle|^2}{E_0 - E_n}. \quad (12)$$

By defining the MS constants of the first and second orders

$$K^{(1)} \equiv -E_0 + K_{\text{SMS}}^{(1)}, \quad (13)$$

$$K^{(2)} \equiv E_0 - K_{\text{SMS}}^{(1)} + K_{\text{SMS}}^{(2)}, \quad (14)$$

we obtain an expression for the mass shift in an isotope  $j$  relative to a hypothetical infinite-mass isotope

$$\Delta E_{\text{MS},j} = K^{(1)} \frac{m}{M_j} + K^{(2)} \frac{m^2}{M_j^2}. \quad (15)$$

Accordingly, the mass shift of an isotope  $i$  with respect to the reference isotope  $a$  is

$$\Delta E_{\text{MS},ia} = K^{(1)} \left( \frac{m}{M_i} - \frac{m}{M_a} \right) + K^{(2)} \left( \frac{m^2}{M_i^2} - \frac{m^2}{M_a^2} \right). \quad (16)$$

It should be noted that, when calculating  $K^{(1)}$  and  $K^{(2)}$  in Sec. IV B and presenting the results in Table I below, we use the experimental values of binding energies as our  $E_0$ . Strictly speaking, experimental energies  $E$  are not equal to the eigenvalues  $E_0$  of the infinite-mass-isotope Hamiltonian; however, the difference  $|E - E_0|$  is negligible for our purposes since the uncertainties of our many-body atomic calculations are much larger.

### B. Field shift

The nuclei of two isotopes differ not only in mass, but also in the parameters of the nuclear charge distribution. Elec-

TABLE I. Mass shift and field shift constants in  $\text{Ca}^+$ , see Eq. (33) and Eqs. (13) and (14); the respective units are described in Sec. IV A, Eqs. (46a) to (46d). Our results for  $\tilde{K}_{\text{SMS}}^{(1)}$  and  $\tilde{F}^{(1)}(R_a)$  are compared with the SMS and FS constants calculated in Refs. [29,30]. The dimensionless nuclear charge radius  $R_a$  [see Eq. (2)] belongs to the  $^{40}\text{Ca}$  isotope. The overall sign of the field-shift constants from Refs. [29,30] was reversed to conform to the definition used in the present work.

Units		4s	4p <sub>1/2</sub>	4p <sub>3/2</sub>	3d <sub>3/2</sub>	3d <sub>5/2</sub>	
$\tilde{K}^{(1)}$	GHz amu	1324	940	951	-1136	-1124	
$\tilde{K}_{\text{SMS}}^{(1)}$	GHz amu	-251	-221	-206	-2487	-2474	
		MBPT+RPA [29]	-259	-204	-200	-2601	-2595
		RCCSD(T) [30]	-243	-208	-204	-2364	-2357
$\tilde{K}^{(2)}$	GHz amu <sup>2</sup>	-3.26	-8.79	-8.78	-3.87	-3.85	
$\tilde{K}_{\text{SMS}}^{(2)}$	GHz amu <sup>2</sup>	-2.53	-8.27	-8.26	-4.49	-4.46	
$\tilde{F}^{(1)}(R_a)$	MHz fm <sup>-2</sup>	266.8	-19.6	-19.9	-112.2	-111.6	
		MBPT+RPA [29]	266.6	-19.6	-19.9	-111.8	-111.2
		RCCSD(T) [30]	263.3	-15.9	-19.5	-93.9	-112.3
$\tilde{F}^{(2)}(R_a)$	kHz fm <sup>-4</sup>	-89.25	6.58	6.65	37.50	37.30	

tronic energy shifts which result from the difference in nuclear charge distribution (or, more precisely, from the difference in nuclear potential) are called field shifts (FS). For the purposes of the present investigation, it is sufficient to assume that all isotopes have the same shape of the nuclear charge distribution and differ only by the values of the charge radii. In this approximation, the electrostatic potential  $V$  of a nucleus depends solely on the nuclear charge radius  $V = V(R)$ ; its total isotopic variation would be  $\delta V_{ia} = V(R_i) - V(R_a)$ . In the second-order perturbation theory, the field shift is given by

$$\Delta E_{\text{FS},ia} = \langle \psi_a | \delta V_{ia} | \psi_a \rangle + \sum_{n \neq a} \frac{|\langle \psi_a | \delta V_{ia} | \psi_n \rangle|^2}{E_a - E_n}. \quad (17)$$

Here  $\psi_a$  is the electronic wave function and  $E_a$  the electronic energy level in the reference isotope  $a$ .

Let  $\delta R_{ia}^2 = R_i^2 - R_a^2$  be the difference between (squares of) dimensionless radii. In Eq. (17), we would like to isolate the dominant first-order field shift  $F^{(1)} \delta R_{ia}^2$  [see Eq. (1)] from other field-shift contributions. To do this, we introduce the standard field-shift operator  $V_{\text{FS}} \equiv \partial V(R) / \partial (R^2)$  and rewrite  $\delta V_{ia}$  as

$$\delta V_{ia} = V_{\text{FS}} \delta R_{ia}^2 + \left( \frac{\delta V_{ia}}{\delta R_{ia}^2} - V_{\text{FS}} \right) \delta R_{ia}^2. \quad (18)$$

Now we can express the first term in Eq. (17) as follows:

$$\langle \psi_a | \delta V_{ia} | \psi_a \rangle = F^{(1)}(R_a) \delta R_{ia}^2 + \delta_{R_i} F^{(1)}(R_a) \delta R_{ia}^2. \quad (19)$$

Here, the first coefficient

$$F^{(1)}(R_a) = \langle \psi_a | V_{\text{FS}} | \psi_a \rangle, \quad (20)$$

is the standard FS constant in Eq. (1). The remaining part of the field shift is the higher-order correction

$$\delta_{R_i} F^{(1)}(R_a) = \left\langle \psi_a \left| \frac{\delta V_{ia}}{\delta R_{ia}^2} - V_{\text{FS}} \right| \psi_a \right\rangle. \quad (21)$$

Since the second term of Eq. (17) is a small correction, one can replace  $\delta V_{ia}$  by  $V_{\text{FS}}$  in it. Hence, we introduce the second-order field-shift electronic constant

$$F^{(2)}(R_a) = \sum_{n \neq a} \frac{|\langle \psi_a | V_{\text{FS}} | \psi_n \rangle|^2}{E_a - E_n}. \quad (22)$$

Finally, we can express the resulting field shift as

$$\Delta E_{\text{FS},ia} = [F^{(1)}(R_a) + \delta_{R_i} F^{(1)}(R_a)] \delta R_{ia}^2 + F^{(2)}(R_a) (\delta R_{ia}^2)^2. \quad (23)$$

Note that the residual potential  $(\delta V_{ia} / \delta R_{ia}^2 - V_{\text{FS}})$  is localized in the nuclear region similarly to the dominant field-shift potential  $V_{\text{FS}}$ . Hence, it makes sense to represent the higher-order correction  $\delta_{R_i} F^{(1)}(R_a)$  as a factor  $f_{\text{ho}}(R_a, R_i)$  multiplied by the field-shift constant

$$\delta_{R_i} F^{(1)}(R_a) = -F^{(1)}(R_a) f_{\text{ho}}(R_a, R_i) 10^{-3}. \quad (24)$$

This form is convenient for presenting the results of our numerical calculation. We will report the numerical results for FS constants  $F^{(1)}(R_a)$ ,  $\delta_{R_i} F^{(1)}(R_a)$ , and  $F^{(2)}(R_a)$  in Sec. IV C.

## C. Additional terms

### 1. Nuclear polarization

Not only the nuclear shape, but also the disposition of a nucleus to be polarized by an electric field changes from isotope to isotope. Nuclear polarization (np) manifests itself in a correction to electronic energy levels; varying nuclear polarization between isotopes thus results in a contribution to isotope shift. Our treatment of the nuclear polarization follows the approach developed in Refs. [23,24]. This approach involves several approximations. First, it neglects the distortion of the nuclear excitation spectrum by the electrons. Second, it discards the transverse part of the interaction between the electron and the nucleus. Within these approximations, the nuclear polarization correction for the electron state  $\zeta$  can be written as [23,24]

$$\Delta E_{\text{np}} = -\alpha \sum_{LM} B(EL) \sum_n \frac{|\langle \zeta | \mathcal{F}_L Y_{LM} | n \rangle|^2}{E_n - E_\zeta + \text{sgn}(E_n) \omega_L}, \quad (25)$$

where  $n$  runs over the complete spectrum of electronic states including the positive and negative continua,  $L$  denotes the multipolarity of nuclear excitations,  $B(EL) = B(EL; L \rightarrow 0)$  are the reduced probabilities of nuclear transitions from the excited (“L”) to the ground state (“0”),  $\omega_L$  are the nuclear excitation energies with respect to the ground state,  $Y_{LM}$  the

spherical harmonics, and  $\mathcal{F}_L$  are characteristic radial functions in the sharp-edge-nucleus approximation [24]

$$\mathcal{F}_{L=0}(r) = \frac{5\sqrt{\pi}}{2r_0^3} \left[ 1 - \frac{r^2}{r_0^2} \right] \theta(r_0 - r), \quad (26)$$

$$\mathcal{F}_{L>0}(r) = \frac{4\pi}{(2L+1)r_0^L} \left[ \frac{r^L}{r_0^{L+1}} \theta(r_0 - r) + \frac{r_0^L}{r^{L+1}} \theta(r - r_0) \right], \quad (27)$$

where  $r_0 = \sqrt{\langle r \rangle^2}$  is the radius of the nuclear sphere and  $\theta$  the step function.

The main contributions to the sum in Eq. (25) arise from two kinds of transitions: giant resonances and lowest-lying rotational transitions. The first are dominant because of their large transition strengths  $B(EL)$ , while the second are enhanced due to the small denominator containing the transition frequency  $\omega_L$ . Accordingly, the dominant low-lying-level contribution to  $\Delta E_{np}$  in the vast majority of even-even nuclei comes from the electric quadrupole transition from the first rotational level to the ground state,  $2^+ \rightarrow 0^+$ .

To facilitate numerical calculations in many-electron systems, we introduce a nuclear polarization potential  $V_{np}$  defined by its matrix elements between single-electron atomic states

$$\langle \zeta | V_{np} | \xi \rangle = -\alpha \sum_{LM} B(EL) \sum_n \frac{\langle \zeta | F_L Y_{LM} | n \rangle \langle n | F_L Y_{LM} | \xi \rangle}{E_n - m + \text{sgn}(E_n) \omega_L}. \quad (28)$$

Here we replace  $E_\zeta$  with electron mass, thereby discarding the (very weak) dependence of  $V_{np}$  on the binding energy of the state  $\zeta$ .

Similarly to the field-shift operator  $V_{FS}$ , the operator  $V_{np}$  is mainly localized in the nuclear region. Hence it is convenient to present the np correction to a given energy level in  $\text{Ca}^+$  as

$$\Delta E_{np} \equiv -g_{np,j} R_j^2 F^{(1)}(R_a) 10^{-3}, \quad (29)$$

where  $R_j$  is the dimensionless nuclear charge radius (2),  $F^{(1)}$  is defined in Eq. (20), and  $g_{np,j}$  is an np coefficient which depends both on the isotope and on the electronic state in question. Accordingly, the *isotope shift* due to nuclear polarization in a given calcium isotope  $i$  with regards to the isotope  $a$  would be

$$\Delta E_{np,ia} = -F^{(1)}(R_a) (R_i^2 g_{np,i} - R_a^2 g_{np,a}) 10^{-3}. \quad (30)$$

The numerical methods for calculating the np coefficients  $g_{np}$  are described in Sec. IV D 2.

## 2. FS and MS cross term

Finally, let us turn to the isotope shift contribution which is a mixture of mass shift and field shift. It is convenient to present it as a nuclear-mass-dependent correction to the field-shift constant. The leading nonrelativistic effect comes from the reduced mass and could be included into the isotope shift by the substitution [25] (see also Ref. [26])

$$F \rightarrow \mu^3 F = F \left( 1 - 3 \frac{m}{M} + \dots \right). \quad (31)$$

In calculating the cross term below, we use  $F^{(1)}(R_a)$  in place of the total  $F$  since the difference between the two cases is

minuscule in the already small cross term

$$\Delta F = -3 \frac{m}{M} F^{(1)}(R_a). \quad (32)$$

Additionally, the contributions of the same order induced by the specific mass-shift operator are expected to be smaller than the reduced-mass effect and are likewise neglected.

## D. General isotope shift formula

The total isotope shift of an energy level consists of mass shift (Sec. II A), field shift (Sec. II B), and additional terms (Sec. II C). Let us denote  $F^{(1)} \equiv F^{(1)}(R_a)$  and  $F^{(2)} \equiv F^{(2)}(R_a)$ ; written as a single sum, the main contributions to the isotope shift between the isotopes  $i$  and  $a$  are

$$\begin{aligned} \Delta E_{ia} = & K^{(1)} \left( \frac{m}{M_i} - \frac{m}{M_a} \right) + K^{(2)} \left( \frac{m^2}{M_i^2} - \frac{m^2}{M_a^2} \right) \\ & + \left[ 1 - f_{ho}(R_a, R_i) 10^{-3} - 3 \left( \frac{m}{M_i} - \frac{m}{M_a} \right) \right] F^{(1)} \delta R_{ia}^2 \\ & - F^{(1)} (R_i^2 g_{np,i} - R_a^2 g_{np,a}) 10^{-3} + F^{(2)} (\delta R_{ia}^2)^2. \end{aligned} \quad (33)$$

## III. MANY-BODY PERTURBATION THEORY

We describe an atom with the relativistic no-pair Dirac-Coulomb Hamiltonian  $H$  which is a sum of the zeroth-order Hamiltonian

$$H_0 = \sum_i [\alpha_i \mathbf{p}_i + \beta_i m + V_{\text{nuc}}(r_i) + U(r_i)], \quad (34)$$

where  $\alpha_i$  and  $\beta$  are the Dirac matrices,  $V_{\text{nuc}}$  is the nuclear Coulomb potential, and the residual electron-electron interaction

$$V_I = \sum_{i<j} \Lambda_{++} I(r_{ij}) \Lambda_{++} - \sum_i \Lambda_+ U(r_i) \Lambda_+. \quad (35)$$

In the later expression,  $\Lambda_{++}$  and  $\Lambda_+$  are the projection operators to the positive-energy part of the Dirac spectrum,  $I$  is the electron-electron interaction operator in the Breit approximation, given by

$$I(r_{ij}) = \frac{\alpha}{r_{ij}} - \frac{\alpha}{2r_{ij}} [\alpha_i \alpha_j + (\alpha_i \hat{\mathbf{r}}_{ij})(\alpha_j \hat{\mathbf{r}}_{ij})], \quad (36)$$

where the first and the second terms correspond to the Coulomb and the Breit interaction, respectively. Here  $\hat{\mathbf{r}} = \mathbf{r}/|\mathbf{r}|$  and  $U$  is a screening potential introduced in the zeroth-order Hamiltonian to partially account for the electron-electron interaction. An important instance of such a potential is the Dirac-Hartree-Fock potential  $V_{\text{HF}}$  whose matrix elements are given by

$$\langle i | V_{\text{HF}} | j \rangle \equiv (V_{\text{HF}})_{ij} = \sum_a I_{ai;aj}, \quad (37)$$

where  $I_{ab;cd} \equiv I_{abcd} - I_{abdc}$ ,  $I_{abcd} \equiv \langle ab | I | cd \rangle$ , and  $I$  is the operator of the electron-electron interaction defined in Eq. (36). Here, we will adopt the standard notation from Ref. [27]: the letters  $a, b, c, \dots$  designate occupied core orbitals;  $n, m, r, \dots$  signify excited orbitals outside the core, including the valence

orbital;  $i, j, k, \dots$  can be either excited or occupied orbitals. The letter  $v$  stands for the valence orbital.

Within the many-body perturbation theory (MBPT), the energy of the valence state  $E_v$  is presented as a perturbation expansion  $E_v = E^{(0)} + E^{(1)} + E^{(2)} + \dots$ . When only the contributions to the valence ionization energy (“val”) are considered, the expansion terms can be obtained [27]

$$E_{\text{val}}^{(0)} = \varepsilon_v, \quad (38a)$$

$$E_{\text{val}}^{(1)} = (V_{\text{HF}} - U)_{vv}, \quad (38b)$$

$$E_{\text{val}}^{(2)} = \sum_{amn} \frac{I_{vamn} I_{mn;va}}{\varepsilon_{av} - \varepsilon_{mn}} - \sum_{abm} \frac{I_{abmv} I_{mv;ab}}{\varepsilon_{ab} - \varepsilon_{vm}} + 2 \sum_{am} \frac{(V_{\text{HF}} - U)_{am} I_{mv;av}}{\varepsilon_a - \varepsilon_m} + \sum_{i \neq v} \frac{(V_{\text{HF}} - U)_{vi} (V_{\text{HF}} - U)_{iv}}{\varepsilon_v - \varepsilon_i}, \quad (38c)$$

where  $\varepsilon_{ab} \equiv \varepsilon_a + \varepsilon_b$ . The expressions for the third-order MBPT correction  $E^{(3)}$  are quite lengthy; they are presented in Ref. [27] and the angular reduction of these formulas is described in Ref. [28]. In practical calculations, it is typical to choose the screening potential  $U$  to be the frozen-core Dirac-Fock potential. In such a case, all terms which include the matrix elements of  $(V_{\text{HF}} - U)$  can be omitted. However, these terms should be preserved if we plan to perturb the above formulas with an additional potential; a perturbation of this kind will be described at the end of this section.

In the present work, we aim to calculate the matrix elements of one-body (field shift) and two-body (specific mass shift) operators. Moreover, we need to compute the second-order iterations of such operators. The simplest way to achieve this is to use the *finite-difference approach*: the perturbing operators are first added to the Hamiltonian and then the numerical derivative with respect to the perturbations is evaluated. Specifically, for calculating the field-shift constants  $F^{(1)}$  and  $F^{(2)}$ , we add the perturbing potential  $V_{\text{FS}}$  with an arbitrary prefactor  $\lambda$  to the nuclear potential, i.e.,  $V_{\text{nuc}} \rightarrow V_{\text{nuc}} + \lambda V_{\text{FS}}$ . Then the valence energies  $E_v(\lambda)$  of the modified Hamiltonian are calculated. Finally, the field-shift constants are obtained by computing numerical derivatives with respect to the parameter  $\lambda$ :

$$F^{(1)} = \left. \frac{\partial E_v(\lambda)}{\partial \lambda} \right|_{\lambda=0}, \quad F^{(2)} = \left. \frac{1}{2} \frac{\partial^2 E_v(\lambda)}{\partial \lambda^2} \right|_{\lambda=0}. \quad (39)$$

Similarly, the specific mass-shift constants  $K_{\text{SMS}}^{(1)}$  and  $K_{\text{SMS}}^{(2)}$  are calculated by adding the perturbing potential  $V_{\text{SMS}}$  to the electron-electron interaction  $I(r_{ij}) \rightarrow I(r_{ij}) + \beta V_{\text{SMS}}(r_{ij})$  and finding the derivative of the perturbed valence energies  $E_v(\beta)$  with respect to  $\beta$ ,

$$K^{(1)} = \left. \frac{\partial E_v(\beta)}{\partial \beta} \right|_{\beta=0}, \quad K^{(2)} = \left. \frac{1}{2} \frac{\partial^2 E_v(\beta)}{\partial \beta^2} \right|_{\beta=0}. \quad (40)$$

The parameters  $\lambda$  and  $\beta$  are chosen in such a way that the resulting changes in energy are much larger than the round-off errors in the numerical calculation, and at the same time, are sufficiently small for the numerical derivative to be stable against variations of  $\lambda$  and  $\beta$ .

In our calculations, we choose the potential  $U$  in the zeroth-order  $H_0$  to be the Dirac-Fock potential. When a perturbation is added to the Hamiltonian  $H_0$  in the finite-difference approach, we can include this perturbation into the self-consistent procedure of computing the Dirac-Fock potential. It was demonstrated in Ref. [31] that such an inclusion is advantageous because it accounts for the infinite sequence of diagrams known as the random-phase-approximation (RPA) corrections, thus yielding a substantial improvement in the accuracy of calculations. We adopt this approach and ensure the self-consistency of the Dirac-Fock potential *after* the perturbation is added to  $H_0$  for each value of the parameters  $\lambda$  and  $\beta$ .

Apart from the finite-difference method, we also implement a more traditional perturbative approach for calculating the first-order matrix elements of one-body operators, specifically, the nuclear polarization correction and the higher-order finite nuclear size correction. Let  $V$  be the one-body potential; we consider the linear-in- $V$  perturbations of the MBPT formulas for energy levels. Accordingly, the perturbations of single-electron energies and wave functions are

$$\varepsilon_i \rightarrow \langle i|V|i \rangle \equiv V_{ii}, \quad |i \rangle \rightarrow |\delta i \rangle = \sum_{k \neq i} \frac{|k \rangle V_{ki}}{\varepsilon_i - \varepsilon_k}. \quad (41)$$

The perturbations of the first two contributions in Eq. (38a) yield

$$\delta E_V^{(0)} = V_{vv}, \quad (42)$$

$$\delta E_V^{(1)} = \sum_{k \neq v} \frac{(V_{\text{HF}} - U)_{vk} V_{kv}}{\varepsilon_v - \varepsilon_k} + 2 \sum_a I_{\delta av;av}. \quad (43)$$

Formulas for the next-order correction  $\delta E_V^{(2)}$  are easily obtained from Eq. (38c) by perturbing all single-electron energies and wave functions according to Eq. (41) and preserving only the part which is linear in  $V$ .

To obtain results equivalent to those delivered by the finite-difference approach, we need to include the contributions from RPA explicitly. This can be achieved by defining the RPA-corrected single-particle matrix elements as [29]

$$V_{an}^{\text{RPA}} = V_{an} + \sum_{bm} \frac{V_{bm}^{\text{RPA}} I_{am;nb} + I_{ab;nm} V_{mb}^{\text{RPA}}}{\varepsilon_b - \varepsilon_m}, \quad (44)$$

and solving the equation iteratively, obtaining the “dressed” single-particle matrix elements  $V_{an}^{\text{RPA}}$ . Then, in the calculation of  $\delta E_V^{(1)}$ , the resulting  $V_{an}^{\text{RPA}}$  are used instead of  $V_{an}$ . We can demonstrate that the first-order RPA iteration accounts for a part of  $\delta E_V^{(2)}$ , while the higher-order RPA iterations correspond to an infinite sequence of higher-order diagrams.

Furthermore, the dressed RPA matrix elements can be implemented in calculations of  $\delta E_V^{(2)}$ , thus accounting for additional sequence of higher-order contributions. Of course, the double-counting terms should be removed from the RPA-corrected  $\delta E_V^{(1)}$  and  $\delta E_V^{(2)}$  contributions. A very similar approach was used in Ref. [29] for the first-order field-shift correction.

TABLE II. Higher-order field-shift and nuclear-polarization contributions for the ground and first excited states of  $\text{Ca}^+$  evaluated with different methods. The methods (i), (ii), and (iii) are described in Secs. IVD 1 and IVD 2. The higher-order field-shift constant correction  $\delta_{R_{46}} F^{(1)} = \delta_{R_{46}} F^{(1)}(R_{40})$  is evaluated for the nuclear charge radii  $r_{40} = 3.4776$  fm and  $r_{46} = 3.4953$  fm [32]; note that  $R_j = r_j/\tilde{\lambda}_C$ . Nuclear polarization correction  $\Delta E_{\text{np}}$  to the electronic energy levels is found for the  $^{40}\text{Ca}^+$  isotope. Units for  $\delta_{R_{46}} F^{(1)}$  are kHz fm $^{-2}$ , while  $\Delta E_{\text{np}}$  is given in MHz.

Method	4s		4p $_{1/2}$		4p $_{3/2}$		3d $_{3/2}$		3d $_{5/2}$	
	$\delta_{R_{46}} F^{(1)}$	$f_{\text{ho}}$								
(i)	-4.810	0.0238	0.642	0.0238	0.645	0.0237	3.814	0.0238	3.794	0.0238
(ii)	-5.354	0.0238	0.452	0.0238	0.456	0.0237	2.011	0.0238	1.998	0.0238
(iii)	-6.202	0.0238	0.447	0.0238	0.453	0.0237	2.519	0.0238	2.506	0.0238
	$\Delta E_{\text{np}}$	$g_{\text{np}}$								
(i)	-0.891	0.364	0.119	0.365	0.119	0.363	0.709	0.366	0.705	0.366
(ii)	-0.991	0.364	0.084	0.365	0.084	0.363	0.374	0.366	0.372	0.366
(iii)	-1.148	0.364	0.083	0.365	0.084	0.363	0.469	0.366	0.466	0.366

#### IV. CALCULATION OF ISOTOPE SHIFT PARAMETERS

##### A. Units

Before we consider the specifics of  $\text{Ca}^+$  numerical calculations, let us briefly discuss the units of isotope shift parameters. According to our definition in Eq. (3), the parameters  $K_{ia}$  and  $F_{ia}$  have units of energy since both  $m/M_j$  and  $R_j^2$  are dimensionless. Such a definition is useful for theoretical treatment, e.g., when we consider the small-parameter expansion in Sec. II A. In the literature, however, the mass-shift constant is expressed in GHz amu and the field shift constant in MHz fm $^{-2}$ . In this case, Eq. (3) would have the following form:

$$\Delta E_{ia} = \tilde{K}_{ia} \left( \frac{1}{M_i} - \frac{1}{M_a} \right) + \tilde{F}_{ia} \delta \langle r^2 \rangle_{ia}. \quad (45)$$

The connection between the two definitions of the isotope-shift constants is as follows:

$$h \tilde{K}^{(1)} = mK^{(1)}, \quad (46a)$$

$$h \tilde{K}^{(2)} = m^2 K^{(2)}, \quad (46b)$$

$$h \tilde{F}^{(1)} = \tilde{\lambda}_c^{-2} F^{(1)}, \quad (46c)$$

$$h \tilde{F}^{(2)} = \tilde{\lambda}_c^{-4} F^{(2)}. \quad (46d)$$

For clarity, here we explicitly included the Planck constant  $h$ . To make our results more accessible for calculating isotope shifts, in Table I we present the numerical results in the form of  $\tilde{K}^{(1)}$ ,  $\tilde{K}^{(2)}$ ,  $\tilde{F}^{(1)}$ , and  $\tilde{F}^{(2)}$ .

It should be mentioned that, in all the calculations reported in this work, we do not include the contributions induced solely by the core electrons: they are the same for all states investigated here and cancel when the transitions between two states are considered.

##### B. Mass shift

Our calculations of the first- and second-order specific-mass-shift constants  $K_{\text{SMS}}^{(1)}$  and  $K_{\text{SMS}}^{(2)}$  are performed with the finite-difference approach described in Sec. III, which reduces the problem at hand to the computation of energies. We included all MBPT corrections to energy up to the third order, i.e., up to the three-photon exchange. This approach accounts

for both the two-photon-exchange corrections to the matrix element of the SMS operator and an infinite sequence of higher-order corrections delivered by the random-phase approximation. The nuclear charge distribution was represented by the two-parameter Fermi distribution model, with the root-mean-square nuclear radii taken from Ref. [32]. The summation over the Dirac spectrum was performed using the finite-basis-set  $B$ -spline method [34]. Actual calculations of the one- and two-photon exchange corrections were performed with  $N = 50$ – $60$  splines of the order 6 and the cavity radius of 35 a.u. The three-photon exchange corrections were computed with  $N = 40$  splines and the partial-wave expansion extended up to  $l = 6$ . The numerical results for the mass-shift constants are presented in Table I. Our values for the first-order constant are in a reasonable agreement with previous calculations [29,30]. For the second-order constants, there are no results reported in the literature.

##### C. Field shift

The calculations of the first- and second-order field-shift constants  $F^{(1)}$  and  $F^{(2)}$  were performed with the finite-difference approach as described in Sec. III. We include MBPT corrections to energy up to the second order, which accounts for all two-photon-exchange corrections to the matrix element of the field-shift operator.

The numerical results for  $F^{(1)}$  and  $F^{(2)}$  are presented in Table I. Our values for the first-order constant  $F^{(1)}$  are in a very good agreement with results by Safronova and Johnson [29]. There is, however, a significant difference with the results of the authors of Ref. [30], especially for 4p $_{1/2}$  and 3d $_{3/2}$  states. The probable reason could be that the numerical approach of Ref. [30] is not particularly suitable for computation of the field shift.

##### D. Additional terms

###### 1. Higher-order field shift

In the present work, we consider three different approaches for evaluating the field-shift correction  $\delta_R F^{(1)}(R_a)$  [see Eq. (21)]. In the order of the improvement of approximation, they are the following: (i) Dirac-Fock including core

TABLE III. The higher-order field shift parameter  $f_{\text{ho}}(R_a, R_i)$  [see Eq. (24),  $A_a = 40$ ] for atomic states of  $\text{Ca}^+$ .

$A_i$	$f_{\text{ho}}(R_a, R_i)$				
	$4s$	$4p_{1/2}$	$4p_{3/2}$	$3d_{3/2}$	$3d_{5/2}$
42	0.0410	0.0411	0.0410	0.0410	0.0410
44	0.0542	0.0543	0.0541	0.0541	0.0541
46	0.0238	0.0238	0.0238	0.0238	0.0238
48	-0.0007	-0.0007	-0.0007	-0.0007	-0.0007

relaxation, based on Eqs. (42) and (43); (ii) random phase approximation (RPA) which relies on adding Eq. (44) to the method (i); and, finally, (iii) MBPT2 + RPA, in which we add a two-photon exchange correction to the method (ii). Table II compares the results for  $\delta_{R_{46}} F^{(1)}(R_{40})$  in  $\text{Ca}^+$  obtained with different methods. In this table, together with the  $\delta_{R_{46}} F^{(1)}(R_{40})$  correction, we display the factor  $f_{\text{ho}}$  which was introduced in Eq. (24). We conclude that, to the level of  $10^{-3}$  relative accuracy, the factor  $f_{\text{ho}}$  is both method independent and the same for all states considered. Our final results for the higher-order field-shift correction are summarized in Table III. One can note that the results obtained are very close to the hydrogenic  $1s$  values. For instance, the hydrogenic result for  $f_{\text{ho}}(R_{46}, R_{40})$  calculated for the  $2s$  state and  $Z = 20$  is 0.02378, which coincides with the values presented in Table III.

## 2. Nuclear polarization

The nuclear polarization correction is induced by the operator  $V_{\text{np}}$  defined in Eq. (28). The single-electron matrix elements of  $V_{\text{np}}$  are calculated in the same way as in our previous work [35]. Specifically, we include the dominant  $E2$  nuclear rotational transition and the giant resonance transitions with  $L = 0, 1, 2, 3$ . For hydrogenic matrix elements we reproduce the results of Ref. [24]. A similar calculation was recently presented in Ref. [36]; the difference is that approximate empirical formulas for  $B(E2)$  were used and only the dominant  $L = 1$  giant resonance was included. Based on Eq. (29), the np correction is conveniently expressed in terms of a  $g_{\text{np}}$  coefficient, which is defined by the ratio of nuclear-polarization and field-shift contributions. While calculating this ratio, it is important to use the same method for both contributions. In such a case, the ratio will not depend on the method of accounting for electron correlations.

The electron-structure corrections to the np effect are calculated with the same approaches as the higher-order field shift in Sec. IV D 1: (i) Dirac-Fock with core relaxation; (ii) RPA; and (iii) MBPT2 + RPA. The numerical results for both quantities  $\Delta E_{\text{np}}$  and  $g_{\text{np}}$  delivered by these three methods for the singly ionized calcium ion  $^{40}\text{Ca}^+$  are listed in Table II. We find that the numerical results expressed in terms of  $g_{\text{np}}$  do not depend on the method of calculation and only weakly depend on the electronic valence state. This is not surprising since it is known that, for light atoms, both the nuclear polarization and the finite nuclear size corrections are roughly proportional to the expectation value of the Dirac  $\delta$  function [37].

We also find that the results for  $g_{\text{np}}$  in  $^{40}\text{Ca}^+$  from Table II are very close to the hydrogenic  $1s$  value  $g_{\text{np}}(1s) = 0.360$ .

The deviation is within 2%, which is much smaller than the uncertainty associated with the approximate treatment of the nuclear polarization effect. Therefore, for many practical purposes, it is sufficient just to use the hydrogenic values of  $g_{\text{np}}$ .

In Table IV we present our results for the nuclear polarization contribution in various isotopes of  $\text{Ca}^+$ . The experimental values of the nuclear quadrupole transition strengths  $B(E2)$  and the excitation energies  $\omega_L$  originate from Ref. [33], while the nuclear charge radii are from Ref. [32].

## E. Numerical results

Our numerical results for the isotope shifts of  $\text{Ca}^+$  isotopes with  $A = 42, 44, 46$ , and  $48$ , relative to the reference isotope  $A_0 = 40$  are summarized in Table V. Note that the numerical results listed in the table do not include a contribution of the electron core that is the same for all states considered and cancels for the transition energies.

The uncertainty of our theoretical values of the mass-shift and field-shift constants stems predominantly from the higher-order electron-correlation effects because all computational errors (basis-set truncation, errors of numerical differentiation) are small. There is no safe way to estimate the omitted electron-correlation effects. To some extent, this can be done by comparing calculations performed by different methods. The specific mass shift is known to be particularly difficult to calculate reliably for many-electron atoms. The agreement of the results obtained by different methods summarized in Table I for  $K_{\text{SMS}}^{(1)}$  is on the level of 10%, which could be taken as an estimation of the uncertainty. Calculations of the field shift can generally be performed to a higher accuracy than for the mass shift. We assume that the uncertainty of our results for  $F^{(1)}$  should be within 5%.

There are no independent calculations to compare with for the second-order isotope shift constants. We assume here that their uncertainties should be comparable with those of the first-order constants  $K_{\text{SMS}}^{(1)}$  and  $F^{(1)}$ . Furthermore, there are uncertainties originating from the nuclear model employed in the calculation of the nuclear polarization effect. We assume these uncertainties to be on the level of 10%, which should be considered as an order-of-magnitude estimate [38,39].

## V. KING PLOTS

### A. Theoretical introduction

The method of King plots [40] is a popular way to analyze the experimentally measured isotope shifts. There are different ways to construct King plots from spectroscopy data to serve similar purposes, see Refs. [3,40]; we will consider the most widely used version. The core idea of a King plot is that, to the leading order, isotope shifts depend linearly on  $m/M_i$  and  $R_i^2$ , see Eq. (1). Hence, if one considers isotope shifts of two different transitions, it is possible to eliminate the poorly known  $R_i^2$  from a system of linear equations. To illustrate this approach, let  $\Delta\nu = \Delta E^{(e)} - \Delta E^{(g)}$  be a transition frequency between an excited and ground atomic energy levels. Then, to the first order

$$\begin{cases} \Delta\nu_{1,ia} = K_{v_1}\mu_{ia} + F_{v_1}\delta R_{ia}^2, \\ \Delta\nu_{2,ia} = K_{v_2}\mu_{ia} + F_{v_2}\delta R_{ia}^2, \end{cases} \quad (47)$$

TABLE IV. Nuclear parameters and the nuclear polarization correction coefficient  $g_{\text{np}}$  [see Eqs. (29) and (30)] for various isotopes of  $\text{Ca}^+$ . The energy of the first nuclear rotational state is  $\omega$ ,  $B(E2)\uparrow$  is the corresponding nuclear transition strength, and  $\sqrt{\langle r^2 \rangle}$  is the root-mean-square nuclear charge radius.

A	$\omega$ [33]	$B(E2)\uparrow$ [33]	$\sqrt{\langle r^2 \rangle}$ [32]	$g_{\text{np}}$				
	[MeV]	[ $e^2\text{b}^2$ ]	[fm]	4s	4p <sub>1/2</sub>	4p <sub>3/2</sub>	3d <sub>3/2</sub>	3d <sub>5/2</sub>
40	3.904	0.010	3.4776	0.3643	0.3646	0.3628	0.3658	0.3660
42	1.525	0.042	3.5081	0.3961	0.3965	0.3945	0.3977	0.3979
44	1.157	0.047	3.5179	0.4122	0.4126	0.4106	0.4139	0.4141
46	1.346	0.018	3.4953	0.4120	0.4123	0.4102	0.4138	0.4140
48	3.832	0.010	3.4771	0.4242	0.4245	0.4224	0.4262	0.4263

with  $\mu_{ia} = (m/M_i - m/M_a)$ . Consequently, we can write a linear relation

$$n_{2,ia} = \frac{F_{\nu_2}}{F_{\nu_1}} n_{1,ia} + \left( K_{\nu_2} - \frac{F_{\nu_2}}{F_{\nu_1}} K_{\nu_1} \right), \quad (48)$$

where  $n_{k,ia} = \Delta v_{k,ia}/\mu_{ia}$  are modified frequencies ( $k = 1, 2$ ). The plot of  $n_{2,ia}$  against  $n_{1,ia}$  for different isotope pairs ( $i, a$ ) is called a King plot (see Fig. 1), and to the first order in isotope shift, it is linear.

The higher-order corrections described in Sec. II and summarized in Eq. (33) distort the linear relation (48). To quantify

TABLE V. Isotope-shift contributions in MHz and kHz, according to Eq. (33), with reference isotope  $A_0 = 40$ . Note that we do not include the large contributions of core electrons to isotope shifts which would be the same for every single-electron state and cancel out when the difference is considered. MS and FS stand for mass shift and field shift, respectively; “sec.” indicates “second order” and “h.o.” means “higher order.” Nuclear polarization contribution is denoted by “np,” while “cross term” means the field- and mass-shift cross term.

A	Isotope shift	Units	4s	4p <sub>1/2</sub>	4p <sub>3/2</sub>	3d <sub>3/2</sub>	3d <sub>5/2</sub>
42	Total	MHz	−1519.6	−1122.9	−1136.5	1329.8	1315.6
	MS	MHz	−1576.5	−1119.2	−1132.8	1353.4	1339.1
	MS, sec.	MHz	0.190	0.511	0.511	0.225	0.224
	FS	MHz	56.8	−4.18	−4.24	−23.9	−23.8
	FS, h.o.	kHz	−2.33	0.172	0.174	0.981	0.975
	FS, sec.	kHz	−4.05	0.299	0.302	1.70	1.69
	Np	kHz	−125.1	9.24	9.31	52.8	52.5
	Cross term	kHz	0.111	−0.008	−0.008	−0.047	−0.047
44	Total	MHz	−2935.1	−2141.7	−2167.7	2553.2	2526.0
	MS	MHz	−3010.4	−2137.1	−2163.1	2584.3	2557.0
	MS, sec.	MHz	0.354	0.955	0.954	0.420	0.418
	FS	MHz	75.2	−5.54	−5.62	−31.6	−31.5
	FS, h.o.	kHz	−4.08	0.301	0.304	1.71	1.70
	FS, sec.	kHz	−7.09	0.523	0.529	2.98	2.96
	Np	kHz	−185.5	13.7	13.8	78.4	78.0
	Cross term	kHz	0.282	−0.021	−0.021	−0.118	−0.118
46	Total	MHz	−4287.2	−3068.2	−3105.5	3695.8	3656.6
	MS	MHz	−4320.5	−3067.1	−3104.4	3709.0	3669.7
	MS, sec.	MHz	0.498	1.34	1.34	0.590	0.587
	FS	MHz	32.9	−2.42	−2.46	−13.9	−13.8
	FS, h.o.	kHz	−0.784	0.058	0.059	0.330	0.328
	FS, sec.	kHz	−1.36	0.100	0.101	0.571	0.568
	Np	kHz	−167.5	12.3	12.4	70.9	70.5
	Cross term	kHz	0.177	−0.013	−0.013	−0.074	−0.074
48	Total	MHz	−5528.5	−3922.6	−3970.3	4746.9	4696.6
	MS	MHz	−5528.0	−3924.4	−3972.1	4745.6	4695.4
	MS, sec.	MHz	0.624	1.68	1.68	0.741	0.737
	FS	MHz	−0.928	0.068	0.069	0.390	0.388
	FS, h.o.	kHz	−0.00065	0.00005	0.00005	0.00027	0.00027
	FS, sec.	kHz	−0.0011	0.0001	0.0001	0.0005	0.0005
	Np	kHz	−192.9	14.2	14.3	81.8	81.2
	Cross term	kHz	−0.0064	0.0005	0.0005	0.0027	0.0027

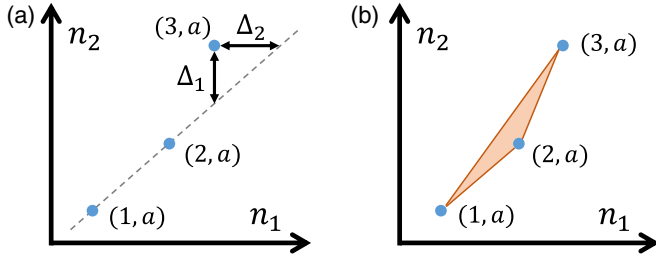


FIG. 1. Two ways to evaluate the nonlinearity of a King plot. Here  $n_{1,2}$  are modified isotope shift frequencies and  $(i, a)$  indicates the isotope pair which corresponds to the given point  $i = 1, 2, 3$  and we assume  $a$  to be the reference isotope  $^{40}\text{Ca}$ . Method (a) characterizes the average difference  $\Delta_{\text{line}} = (\Delta_1 + \Delta_2)/2$  between the outlier point and the line defined by the two other points. Method (b) quantifies the area of the triangle defined by the three points, see Eq. (51) and Ref. [2].

this deviation from linearity, we will apply two different methods shown schematically in Fig. 1. The first method relies on averaging the difference between the outlier point and the line defined by two other points

$$\Delta_{\text{line}} = (\Delta_1 + \Delta_2)/2, \quad \Delta_{1,2} > 0. \quad (49)$$

To scale  $\Delta_{\text{line}}$  back to frequency units, we multiply its value by  $|m/M_j - m/M_a|$ , where  $(j, a)$  is the isotope pair of the outlier point. The second method considers the area of a triangle defined by three points of a King plot [2]. To formalize this approach, we need to define the ‘‘isotope shift vectors’’ whose coordinates correspond to modified frequency shifts in different isotope pairs

$$\vec{n}_k = (n_{k,1a}, n_{k,2a}, n_{k,3a}). \quad (50)$$

The area of the King-plot triangle can be calculated as [2,11]

$$\Delta_{V_2} = \frac{1}{2} \det(\vec{n}_1, \vec{n}_2, \vec{\mathbb{1}}_3), \quad (51)$$

where  $\vec{\mathbb{1}}_3 \equiv (1, 1, 1)$ . Again, to scale  $\Delta_{V_2}$  to frequency units, we multiply it by the second power of the mean value  $\overline{|m/M_i - m/M_a|}^2$ , where  $(i, a)$  are all four isotope pairs.

The later approach is easily generalized to include more isotopes and more transitions [11]. For instance, the isotope shifts in  $\text{Ca}^+$  can be measured in four pairs of isotopes: the reference  $A = 40$  and each of the  $A = 42, 44, 46, 48$  isotopes. In this way, we would obtain four-dimensional isotope-shift vectors

$$\vec{n}_k = (n_{k,1a}, n_{k,2a}, n_{k,3a}, n_{k,4a}). \quad (52)$$

The nonlinearity is defined by

$$\Delta_{V_3} = \frac{1}{6} \det(\vec{n}_1, \vec{n}_2, \vec{n}_3, \vec{\mathbb{1}}_4), \quad (53)$$

where  $\vec{\mathbb{1}}_4 = (1, 1, 1, 1)$ . We scale  $\Delta_{V_3}$  back to frequency units by introducing the mean-value factor  $\overline{|m/M_i - m/M_a|}^3$ , where  $(i, a)$  are all four isotope pairs. This case corresponds to a three-dimensional King plot.

In the present work we analyze nonlinearities both for the two- and three-dimensional (2D) King plots. In the first case, we consider two sets of isotopes:  $(A_i, 40)$  with  $A_i = 42, 44, 46$ , and  $A_i = 42, 44, 48$ . Note that the charge radii of  $^{40}\text{Ca}$

TABLE VI. Two-dimensional King-plot NLs. Methods (a) and (b) are depicted in Fig. 1. The NL units are Hz for method (a) and  $\text{kHz}^2$  for method (b). The ‘‘3<sup>rd</sup> point’’ column corresponds to the isotope shifts in  $A = 42, 44, 46$  isotopes and the ‘‘4<sup>th</sup> point’’ to the isotope shifts in  $A = 42, 44, 48$  isotopes with respect to  $A_a = 40$ . Approximate percentages of each higher-order term contribution to the total NLs are given in the respective columns. The abbreviations for the individual terms are the same as in Table V.

Transitions	Contribution	3 <sup>rd</sup> point		4 <sup>th</sup> point	
		(a)	(b)	(a)	(b)
$3d_{3/2} \rightarrow 4s$	total	44	$1.1 \times 10^3$	180	$3.3 \times 10^3$
	MS, Sec.	99.2%	99.2%	24.7%	24.7%
	FS, h.o.	0.1%	0.1%	0.0%	0.0%
	FS, sec.	0.6%	0.6%	0.2%	0.2%
	Np	0.2%	0.2%	75.1%	75.0%
Cross term	0.0%	0.0%	0.0%	0.0%	
$4p_{1/2} \rightarrow 4s$	Total	$1.4 \times 10^4$	$2.8 \times 10^5$	$1.4 \times 10^4$	$2.2 \times 10^5$
$3d_{5/2} \rightarrow 4s$	MS, sec.	99.7%	99.7%	99.5%	99.5%
	FS, h.o.	0.1%	0.1%	0.1%	0.1%
	FS, sec.	0.0%	0.0%	0.1%	0.1%
	Np	0.2%	0.2%	0.3%	0.3%
	Cross term	0.0%	0.0%	0.0%	0.0%

and  $^{48}\text{Ca}$  are almost equal, while the radii of the  $A = 42, 44, 46$  isotopes are larger than both, as can be seen from Table IV; this fact may influence the pattern of King-plot nonlinearity in a way that is specific for calcium.

## B. King-plot nonlinearity in $\text{Ca}^+$

We calculate two-dimensional King-plot nonlinearities (NLs) with the two methods illustrated in Fig. 1, for two pairs of transitions:  $(3d_{3/2} \rightarrow 4s; 3d_{5/2} \rightarrow 4s)$  and  $(4p_{1/2} \rightarrow 4s; 3d_{3/2} \rightarrow 4s)$ . The first pair consists of two narrow transitions and is suitable for the search of possible new-physics effects [18]. However, this transition pair poses a challenge for theoretical predictions of NLs, as it involves significant cancellations between the isotope shifts. On the other hand, the second pair of transitions does not have such strong cancellations, and consequently, is better suited for detecting King-plot nonlinearities originating from the standard model, as will be discussed below.

Since there are four isotope pairs available for  $\text{Ca}^+$  (four points on a 2D King plot) we calculate NLs both for the ‘‘third point’’ ( $A = 42, 44, 46$  versus  $A = 40$ ) and the ‘‘fourth point’’ ( $A = 42, 44, 48$  versus  $A = 40$ ). Additionally, we determine the three-dimensional (3D) King plot NL as defined in Eq. (53) for the following set of transitions:  $3d_{3/2} \rightarrow 4s$ ,  $3d_{5/2} \rightarrow 4s$ , and  $4p_{1/2} \rightarrow 4s$ .

Our numerical results are presented in Tables VI and VII for the NL of the 2D and 3D King plots, respectively. Individual contributions to the 2D NL are roughly additive; in Table VI we present the total NL results as well as the individual contributions expressed in a percentage of the total values. On the other hand, individual contributions to the 3D NL turn out to be nonadditive. So we successively *exclude* each of the terms and list the resulting change of NL values in Table VII.

TABLE VII. The three-dimensional King plot NLs, see Eq. (53). Contributions to the three-dimensional NL are nonadditive; we consecutively *exclude* each term from the total sum and record how the NL value is impacted. The second column names the one term excluded from the sum, whereas the third column shows the *change* of the NL in percentage of the “total” value with all terms included. The abbreviations for the individual terms are the same as in Table V.

Transitions	Contribution	NL[kHz <sup>3</sup> ]
$4p_{1/2} \rightarrow 4s$ ;	Total	$8.2 \times 10^3$
$3d_{3/2} \rightarrow 4s$ ;	No MS, sec.	99.9%
$3d_{5/2} \rightarrow 4s$ .	No FS, h.o.	0.0%
	No FS, sec.	0.0%
	No np	99.9%
	No cross term	0.0%

Examining individual contributions to NL, we observe that the second-order and higher-order FS corrections and the cross term are essentially negligible for  $\text{Ca}^+$  and can be omitted in future studies. This was expected since the nuclear-size effects tend to be small for light atoms. The main source of NL in  $\text{Ca}^+$  is the second-order mass shift, which is consistent with our previous findings for argon [25]. Quite surprisingly, however, we find a large contribution from the nuclear polarization for the fourth-point ( $3d_{3/2}, 3d_{5/2} \rightarrow 4s$ ) 2D King-plot and for the 3D King plot. A possible reason is the irregular behavior of the nuclear charge radii: the charge radii of  $^{40}\text{Ca}$  and  $^{48}\text{Ca}$  are almost equal, whereas the radii of  $^{42,44,46}\text{Ca}$  are larger than both of them (see Table IV).

One might notice that the methods (a) and (b) produce NLs that are, first, of different units and, second, very different numerically. This is not surprising since method (a) measures a linear distance whereas method (b) measures the area of a triangle. Naturally, both methods describe the same phenomenon and thus the resulting NLs correspond to the same experimental uncertainty, which would allow to detect them. We checked this numerically by a Monte Carlo simulation and confirmed that the experimental errors at which the NLs become visible is the same for the (a) and (b) methods of the NL determination.

We now address the question of how accurately the present theory can predict the NLs of King plots within the standard model. Theoretical accuracy of isotope-shift (particularly, the specific mass shift) constants of many-electron systems achievable in modern calculations is not very high (on the level of few percent). Initially, it was assumed that, because the NLs are very small, even an approximate theoretical result would provide valuable information for searching for new physics with Kings plots. However, as has been shown in our previous work [26], the numerical values of NLs in hydrogen-like ions turn out to be very sensitive to the experimental uncertainties of the nuclear charge radii, which places limits on theoretical predictions of NLs. In the present work, we studied the sensitivity of the numerical values of NLs in  $\text{Ca}^+$  to the theoretical uncertainties of isotope-shift parameters and to the experimental errors of nuclear charge radii. Since the standard methods of error propagation do not work in this case, we used a Monte Carlo simulation. Each of the computed isotope-shift constants was represented by a set of

TABLE VIII. NLs and their uncertainties for the two-dimensional King plots. For each entry, the upper line shows a NL calculated with method (a) and its uncertainties, while the lower line gives the maximal experimental uncertainties of (both) transition frequencies that allow to detect the NL values listed in the upper line.  $\epsilon_{\text{const.}}$  is the theoretical error of the NL value stemming from the numerical uncertainty of isotope-shift constants, whereas  $\epsilon_{\text{radii}}$  is the NL uncertainty originating from the experimental values of nuclear charge radii. The units are kHz.

Transitions		Value	$\epsilon_{\text{const.}}$	$\epsilon_{\text{radii}}$
$3d_{3/2} \rightarrow 4s$ ;	3 <sup>rd</sup> point	0.044	1.5	0.013
$3d_{5/2} \rightarrow 4s$ .		(0.005)	(0.20)	(0.002)
	4 <sup>th</sup> point	0.181	1.5	0.023
		(0.012)	(0.12)	(0.002)
$4p_{1/2} \rightarrow 4s$ ;	3 <sup>rd</sup> point	14	2.4	4.0
$3d_{3/2} \rightarrow 4s$ .		(1.3)	(0.3)	(0.45)
	4 <sup>th</sup> point	14	2.5	7.0
		(0.8)	(0.17)	(0.4)

quasirandom normally distributed numbers, with parameters of the normal distribution defined by the central value and the uncertainty of the corresponding isotope-shift constant. The NL errors were obtained by analyzing the resulting distributions of the NL values. The uncertainty estimates described in Sec. IV E were employed for the isotope-shift constants. For the nuclear charge radii, we used the errors from Ref. [32], specifically the systematic uncertainty of 0.0020 fm for all isotopes and the relative uncertainty of 0.0009 fm of nuclear charge radii of isotopes  $A = 42, 44, 46$ , and 48 relative to  $A = 40$ .

The numerical results are summarized in Table VIII. The two methods of the NL determination yield very similar results, therefore, it is sufficient to present the values only for method (a). We find that for the ( $3d_{3/2}, 3d_{5/2} \rightarrow 4s$ ) pair the theoretical uncertainty  $\epsilon_{\text{const}}$  is an order of magnitude larger than the central value. This is not surprising given the strong cancellations between the isotope shifts of the two transitions. As is evident from Table V, we cannot reliably predict the isotope shift of the  $3d_{5/2}-3d_{3/2}$  fine-structure difference, and this fact leads to a large uncertainty in the corresponding NLs. Hence, for the ( $3d_{3/2}, 3d_{5/2} \rightarrow 4s$ ) pair only an upper limit of NL can be obtained: we conclude that the standard-model NLs for this transition pair in  $\text{Ca}^+$  might be observed when the experimental accuracy is below 200 Hz. As a matter of fact, such accuracy is already achievable in modern experiments with  $\text{Ca}^+$  [16,18], although no confirmed NLs have been reported so far.

The second pair of transitions considered in this work ( $4p_{1/2} \rightarrow 4s$ ;  $3d_{3/2} \rightarrow 4s$ ) involves transitions with different principal quantum numbers  $n$ , hence the cancellation between the isotope shifts is much weaker. Accordingly, the NLs predicted for this KP transition pair are significantly larger and can be seen already at the experimental accuracy of about 1.5 kHz. The purely theoretical uncertainty (which stems from the uncertainty of isotope-shift constants) amounts to  $\sim 20\%$  of the NL value, which means that, in this case, our theory can quantitatively predict a NL. Additionally, the nuclear-radii

uncertainty turns out to be about twice as large as the purely theoretical one. This means that, if observed, the ( $4p_{1/2} \rightarrow 4s$ ;  $3d_{3/2} \rightarrow 4s$ ) King plot can be used to improve our knowledge of nuclear charge radii.

## VI. CONCLUSION

We performed a detailed study of isotope shifts in  $\text{Ca}^+$  transition energies. The calculations of the first-order mass-shift and field-shift isotope-shift constants were carried out within the relativistic many-body perturbation theory for the  $4s$ ,  $4p_{1/2, 3/2}$ , and  $4d_{3/2, 5/2}$  states of  $\text{Ca}^+$ . The results are in good agreement with the previous calculations which were performed using many-body perturbation theory [29] and the coupled-cluster method [30].

The higher-order isotope-shift effects responsible for the standard-model (SM) nonlinearities in King plots were calculated: second-order mass shift, second- and higher-order field shifts, and nuclear polarization. We analyzed the resulting Kings-plot nonlinearities in  $\text{Ca}^+$  with three different methods and demonstrated that the dominant contributions originate from the second-order mass shift and nuclear polarization.

Two pairs of transitions were examined in this work. The first pair, ( $3d_{3/2} \rightarrow 4s$ ;  $3d_{5/2} \rightarrow 4s$ ), consists of two narrow transitions that can be measured very accurately, which makes it suitable for new-physics searches with King plots. However, for this pair the present theory can only predict an upper limit of the nonlinearities caused by the SM effects, owing to large cancellations between the isotope shifts. Based on our results,

we conclude that the SM nonlinearities in this transition pair can become visible when the experimental accuracy is below 200 Hz, an accuracy already achieved in modern experiments with  $\text{Ca}^+$  [16–18]. So, as long as experiments do not detect any King-plot nonlinearity, this fact can be used for placing bounds on possible new-physics effects, see Ref. [2]. However, as soon as the King plot is measured to be nonlinear, it would be hard to discern whether this nonlinearity is due to a SM effect or a new-physics interaction.

The second transition pair investigated in this work, ( $4p_{1/2} \rightarrow 4s$ ;  $3d_{3/2} \rightarrow 4s$ ), involves two very different transitions. The line profile of the  $4p$ – $4s$  transition is rather wide and cannot be measured as accurately as the  $3d$ – $4s$  one. However, the cancellation between the isotope shifts is relatively small in this case and the theory can provide a quantitative prediction of the SM nonlinearity. As follows from Table VIII, the King-plot nonlinearity for this transition pair can be observed already at the 1-kHz level of experimental uncertainty, which is feasible in modern experiments. We conclude that the ( $4p_{1/2} \rightarrow 4s$ ;  $3d_{3/2} \rightarrow 4s$ ) transition pair is a promising candidate for the experimental identification of the SM King-plot nonlinearity and for obtaining information about nuclear charge radii.

## ACKNOWLEDGMENT

This work was funded by the Deutsche Forschungsgemeinschaft (DFG, German Research Foundation) under Germany's Excellence Strategy–EXC-2123 QuantumFrontiers–390837967 and under Project No. SU 658/4-2.

- 
- [1] M. S. Safronova, D. Budker, D. DeMille, D. F. J. Kimball, A. Derevianko, and C. W. Clark, *Rev. Mod. Phys.* **90**, 025008 (2018).
  - [2] J. C. Berengut, D. Budker, C. Delaunay, V. V. Flambaum, C. Frugiele, E. Fuchs, C. Grojean, R. Harnik, R. Ozeri, G. Perez *et al.*, *Phys. Rev. Lett.* **120**, 091801 (2018).
  - [3] I. Counts, J. Hur, D. P. L. Aude Craik, H. Jeon, C. Leung, J. C. Berengut, A. Geddes, A. Kawasaki, W. Jhe, and V. Vuletić, *Phys. Rev. Lett.* **125**, 123002 (2020).
  - [4] P. O. Schmidt, T. Rosenband, C. Langer, W. M. Itano, J. C. Bergquist, and D. J. Wineland, *Science* **309**, 749 (2005).
  - [5] D. J. Wineland, J. C. Bergquist, J. J. Bollinger, R. E. Drullinger, and W. M. Itano, in *Frequency Standards and Metrology* (World Scientific, Singapore, 2002), pp. 361–368.
  - [6] S. A. King, L. J. Spieß, P. Micke, A. Wilzewski, T. Leopold, E. Benkler, R. Lange, N. Huntemann, A. Surzhykov, and V. A. Yerokhin, *Nature (London)* **611**, 43 (2022).
  - [7] A. D. Ludlow, M. M. Boyd, J. Ye, E. Peik, and P. O. Schmidt, *Rev. Mod. Phys.* **87**, 637 (2015).
  - [8] N. Picqué and T. W. Hänsch, *Nat. Photon.* **13**, 146 (2019).
  - [9] M. G. Kozlov, M. S. Safronova, J. R. Crespo López-Urrutia, and P. O. Schmidt, *Rev. Mod. Phys.* **90**, 045005 (2018).
  - [10] C. Delaunay, R. Ozeri, G. Perez, and Y. Soreq, *Phys. Rev. D* **96**, 093001 (2017).
  - [11] J. C. Berengut, C. Delaunay, A. Geddes, and Y. Soreq, *Phys. Rev. Res.* **2**, 043444 (2020).
  - [12] G. W. F. Drake, H. S. Dhindsa, and V. J. Marton, *Phys. Rev. A* **104**, L060801 (2021).
  - [13] J. Hur, D. P. L. Aude Craik, I. Counts, E. Knyazev, L. Caldwell, C. Leung, S. Pandey, J. C. Berengut, A. Geddes, W. Nazarewicz *et al.*, *Phys. Rev. Lett.* **128**, 163201 (2022).
  - [14] N. L. Figueroa, J. C. Berengut, V. A. Dzuba, V. V. Flambaum, D. Budker, and D. Antypas, *Phys. Rev. Lett.* **128**, 073001 (2022).
  - [15] S. O. Allehabi, V. A. Dzuba, V. V. Flambaum, and A. V. Afanasjev, *Phys. Rev. A* **103**, L030801 (2021).
  - [16] F. W. Knollmann, A. N. Patel, and S. C. Doret, *Phys. Rev. A* **100**, 022514 (2019).
  - [17] F. W. Knollmann, A. N. Patel, and S. C. Doret, *Phys. Rev. A* **107**, 069902(E) (2023).
  - [18] C. Solaro, S. Meyer, K. Fisher, J. C. Berengut, E. Fuchs, and M. Drewsen, *Phys. Rev. Lett.* **125**, 123003 (2020).
  - [19] F. Gebert, Y. Wan, F. Wolf, C. N. Angstmann, J. C. Berengut, and P. O. Schmidt, *Phys. Rev. Lett.* **115**, 053003 (2015).
  - [20] P. Müller, K. König, P. Imgram, J. Krämer, and W. Nörtershäuser, *Phys. Rev. Res.* **2**, 043351 (2020).
  - [21] I. I. Tupitsyn, V. M. Shabaev, J. R. Crespo López-Urrutia, I. Draganić, R. S. Orts, and J. Ullrich, *Phys. Rev. A* **68**, 022511 (2003).
  - [22] W. R. Johnson, *Atomic Structure Theory* (Springer, Berlin, 2007).

- [23] G. Plunien, B. Müller, W. Greiner, and G. Soff, *Phys. Rev. A* **43**, 5853 (1991).
- [24] A. V. Nefiodov, L. N. Labzowsky, G. Plunien, and G. Soff, *Phys. Lett. A* **222**, 227 (1996).
- [25] V. A. Yerokhin, K. Pachucki, and V. Patkóš, *Ann. Phys. (Leipzig)* **531**, 1800324 (2019).
- [26] V. A. Yerokhin, R. A. Müller, A. Surzhykov, P. Micke, and P. O. Schmidt, *Phys. Rev. A* **101**, 012502 (2020).
- [27] S. A. Blundell, D. S. Guo, W. R. Johnson, and J. Sapirstein, *At. Data Nucl. Data Tables* **37**, 103 (1987).
- [28] W. R. Johnson, S. A. Blundell, and J. Sapirstein, *Phys. Rev. A* **37**, 2764 (1988).
- [29] M. S. Safronova and W. R. Johnson, *Phys. Rev. A* **64**, 052501 (2001).
- [30] A. Dorne, B. K. Sahoo, and A. Kastberg, *Atoms* **9**, 26 (2021).
- [31] J. C. Berengut, V. A. Dzuba, and V. V. Flambaum, *Phys. Rev. A* **68**, 022502 (2003).
- [32] I. Angeli and K. P. Marinova, *At. Data Nucl. Data Tables* **99**, 69 (2013).
- [33] S. Raman, C. W. Nestor, and P. Tikkanen, *At. Data Nucl. Data Tables* **78**, 1 (2001).
- [34] V. M. Shabaev, I. I. Tupitsyn, V. A. Yerokhin, G. Plunien, and G. Soff, *Phys. Rev. Lett.* **93**, 130405 (2004).
- [35] R. A. Müller, V. A. Yerokhin, A. N. Artemyev, and A. Surzhykov, *Phys. Rev. A* **104**, L020802 (2021).
- [36] V. V. Flambaum, I. B. Samsonov, H. B. Tran Tan, and A. V. Viatkina, *Phys. Rev. A* **103**, 032811 (2021).
- [37] M. Puchalski, A. M. Moro, and K. Pachucki, *Phys. Rev. Lett.* **97**, 133001 (2006).
- [38] I. A. Valuev, Ph.D. thesis, Ruprecht-Karls-Universität Heidelberg, 2022.
- [39] I. A. Valuev (private communication).
- [40] W. H. King, *Isotope Shifts in Atomic Spectra* (Springer Science & Business Media, New York, 2013).